Impact hammer testing on post-tensioned steel rectangular hollow sections; an investigation into the "compression-softening" effect

Darragh Noble[a,*], Dr. Maria Nogal[a], Dr. Alan O'Connor[a], Dr. Vikram Pakrashi[b]

[a] *Dept. of Civil, Structural & Environmental Engineering, Museum Building, Trinity College Dublin, College Green, Dublin 2, Ireland.*
[b] *Dynamical Systems & Risk Laboratory, Dept. of Civil & Environmental Engineering, School of Engineering, University College Cork, College Road, Cork, Ireland.*

Abstract

This paper describes the outcome of steel impact hammer testing on externally axially loaded steel rectangular hollow sections (RHSs) and compares the response to that of post-tensioned RHSs. Both the fundamental natural bending frequency of the beam sections and the corresponding damping ratios have been calculated from the measured dynamic response of the beam to a series of impact hammer strikes. The purpose of the research is to test the validity of the *"compression-softening"* effect for post-tensioned sections and to determine on a phenomenological level if an external axial load is dynamically equivalent to a post-tensioning load. The implications of the research are vast, as currently, some authors suggest that "compression-softening" is applicable to pre- and post-tensioned concrete members. The validity of this argument shall be put to the test in this paper. The fundamental bending frequencies have been calculated through a signal processing regime followed by Fast Fourier Transforms (FFTs) and a peak picking algorithm applied to the dynamic output data obtained from an accelerometer affixed to the beam sections. The damping ratio has been calculated using the half-power bandwidth method. The bending frequencies have been calculated repeatedly while changing the axial load level and the subsequent changes in both frequency and damping ratio, with increasing axial load level have been anal-

*Corresponding author
Email address: nobleda@tcd.ie (Darragh Noble)

ysed to determine if the results are statistically significant.

Keywords: Modal testing, Signal Processing, Fast Fourier transform, Half-power bandwidth, External Axial Load, Post-tensioning, Euler buckling, Compression softening, Natural bending frequency, Damping ratio.

1. Introduction

The prediction of the change in natural vibration frequencies with varying prestress force magnitude for prestressed concrete (PSC) structures is a particularly important problem. This problem has implications particularly in the field of PSC bridge girders and more recently for post-tensioned concrete wind turbine towers, both of which are structures that are susceptible to extreme dynamic excitation. To date, the effect of applied prestressing force on the dynamic behaviour of pre- and post- tensioned structures has been a widely debated topic [1]. There are currently three distinct arguments to be found in the literature;

1. The natural vibration frequencies (NFs), ω_n, of PSC structures tend to decrease as the magnitude of the pre-stressing force is increased. This is known as the *"compression-softening"* effect and is based on classical Euler-Bernoulli beam theory of an externally axially loaded homogeneous beam [2, 3, 4, 5, 6, 7, 8]. It is limited in that it only takes into account Kirchoff's kinematic modelling and is based on small deflection theory only. It does not allow for large displacements and moderate rotations.

2. NFs of PSC structures are unaffected by pre-stress force magnitude. This argument has been taken to the fore by Hamed & Frostig [9], who present a non-linear kinematic model and conclude that the final equation of motion for the vibrating beam system is independent of the prestress force magnitude, and consequently that the natural vibration frequency of PSC structures is not affected by the magnitude of the prestressing force.

3. NFs of PSC structures tends to increase as the magnitude of the pre-stressing force is increased. This has found to be the case in numerous empirical studies, conducted [10, 11, 12] however, a satisfactory

mathematical model predicting the increase in NFs with increasing pre-stressing force has yet to be formulated, despite some attempts [12, 13].

~~The importance of this research is widespread.~~ The effect of prestress force magnitude on natural frequency of PSC structures has many implications, specifically in the PSC bridge industry and for pre-cast, post-tensioned concrete wind turbine towers. Prestress force decreases over time due to concrete creep, steel relaxation, anchorage pull in and other factors. Structural engineers should thus be able to monitor or estimate changes in the natural bending frequency of PSC structures over the course of their design life to ensure their safety and serviceability. As a result, prediction of change in natural frequency of PSC structures over time is of great importance.

In order to isolate this problem, a study must first be conducted into the validity of the aforementioned *"compression-softening"* effect. Subsequently, the aim of this paper is to report on the impact hammer testing and experimental modal analysis conducted on both externally axially loaded steel rectangular hollow sections (RHSs), and their post-tensioned counterparts. The purpose of the research is first to determine under what conditions *"compression-softening"* theory holds true. The assumption that an external axial load is dynamically equivalent to an internal post-tensioning force is investigated in this paper. This paper has been adapted and expanded from a conference paper previously published by the same authors [14].

This paper is organised as follows; Section 2 presents a literature review of the current arguments used to describe the change in natural bending frequency with increasing pre- and post-tensioning force for PSC structures, and also outlines the theory behind the *"compression-softening"* effect. Section 3 describes the experimental set-up in the laboratory, for both static and dynamic tests conducted. Section 4 describes the signal processing processed ~~invoked~~ on the obtained data, and the calculation of the fundamental bending frequencies and damping ratios for the given beam and load case combinations. Section 5 describes the experimental results obtained, and describes the observed changes in fundamental natural bending frequency and damping ratio with increasing axial load level. Section 6 outlines the main conclusions of the paper derived from the experimental results. Appendix A outlines the results of statistical analysis on the obtained results by regressing both fundamental natural bending frequency and damping ratio on axial load level~~, and determine if the observed changes are statistically significant.~~

2. Literature Review

2.1. Frequency decreases with increasing prestressing force

Many authors have argued that NFs of PSC structures tends to decrease as the magnitude of the pre-stressing force increases [2, 3, 4, 5, 6]. Various mathematical models have been formulated, based on a linear kinematic framework (*"Kirchhoff's kinematic model"*) highlighting this. It considers small deflection theory only and does not take into account large displacements and moderate rotations about the axis of bending. The *"compression-softening"* equation, as first outlined in [2], is given as;

$$\omega_n = \sqrt{\left(\frac{n\pi}{\ell}\right)^4 \frac{EI}{m} - \left(\frac{n\pi}{\ell}\right)^2 \frac{N}{m}} \tag{1}$$

where ω_n is the natural frequency of the beam in radians per unit time, n is the mode number, ℓ is the span length, N is the axial compressive force (positive), m is the beam mass per unit length, E is Young's modulus of elasticity and I is the second moment of area, with respect to the centroid of the cross section.

There are arguments suggesting that this *"compression-softening"* effect is not valid for PSC structures. Firstly, the main assumptions in [2, 3, 4, 5, 6] take into account an external axial load being applied to a homogeneous section. In the case of pre-stressed concrete, neither of these assumptions are valid. According to some authors [15, 16, 17], *"compression-softening"* is only applicable to external axial loads and the pre-stressing force cannot be considered as such as it is internal to the structure. Furthermore, as pointed out by Saiidi et al. [10], concrete is not a homogeneous material and is susceptible to cracks, and it was shown experimentally that the application of Equation 1 to PSC beams is erroneous.

Equation 1 is based on Euler buckling theory, which is only applicable to homogeneous externally axially loaded beams, such as steel beams. The main assumption of applying the *"compression-softening"* effect is that the pre-stressing force in the strand is equivalent to an external axial load of equal magnitude applied to the beam ends. This has been refuted by many authors who state that the prestressing force is not equivalent to an externally applied axial load as it is internal to the structure and as a result cannot cause Euler buckling to occur [4, 16, 17, 18]. This shall be investigated at length in this paper.

2.2. No change in frequency with increasing prestressing force

Hamed & Frostig [9] presented a rigorous mathematical proof indicating that the magnitude of the pre-stressing force does not affect the NFs of PSC beams. A non-linear kinematic framework was adopted, in comparison with the aforementioned linear kinematic framework presented in other studies [2, 4, 5, 6]. This enabled large displacements and moderate rotations to be accounted for. It was subsequently mathematically demonstrated that the governing equation of motion (vibration equation) for the beam is independent of axial force, for bonded and unbonded pre-stressing tendons. Dall'Asta & Dezi [19] through mathematical modelling, Kerr [20], through mathematical modelling backed up by experimental testing and Dai & Chen [8], through a finite element analysis all concluded that there was a change in NFs with varying pre-stressing force, however, they suggested that the magnitude of the change is negligible and subsequently concur with Hamed & Frostig [9] in stating that the magnitude of the pre-stress force has no effect on the NFs of PSC structures, within practical ranges of pre-stressing force. Other authors [17, 18] also concur with this, however, their respective discussions are not backed up by any form of mathematical or experimental evidence.

2.3. Frequency increases with increasing prestressing force

Experimental evidence is relatively abundant to suggest that the NFs of PSC structures actually increases with increasing magnitude of pre-stressing force [10, 11, 12, 21, 22, 23, 24]. Experimental modal analysis has been conducted on a series of vibration tests, both in-situ and in the laboratory indicating that NFs increase with increasing pre-stressing force. Saiidi et al. [10], who initially assumed the *"compression softening"* argument to hold true for PSC beams, suggest the reason behind this is due to the effect of the pre-stressing force on the closure of micro-cracks that have been induced in the PSC section, and the subsequent increase in stiffness in the section as a result. However, this has not been proven conclusively, either experimentally or theoretically. Mathematical models have also been formulated indicating the increase in NFs with increasing pre-stressing force [12, 13].

Furthermore, there is significant evidence to suggest that the NFs of PSC structures is not only sensitive to the magnitude of the prestressing force but is also sensitive to the tendon profile within the section and the tendon eccentricity [4, 5, 11]. The tendon profile and eccentricity alters the net second moment of area of the cross section, thus directly affecting the bending

stiffness and hence NF of the beam section. The models tracking an increase in NF with increasing pre-stressing force tend to focus on stiffness alteration, or the increase in flexural rigidity, EI, of the section with increasing pre-stressing force.

2.4. Compression Softening

The *"compression-softening"* argument was put forward by Tse et al. [2]. It is valid for externally axially loaded Euler-Bernoulli beams that are susceptible to buckling failure. The theory is based on Euler buckling theory and states that the closer a beam gets to its Euler buckling load, P_{cr}, the less stiff the beam becomes in bending, and thus the NFs of the beam are decreased. Through the assumption of undamped simple harmonic motion, the appropriate boundary conditions, and the appropriate mode shapes of vibration for a simply supported beam, it can be shown that the n^{th} natural bending frequency of such a beam under axial tension is given as [2];

$$\omega_n = \sqrt{\left(\frac{n\pi}{\ell}\right)^2 \frac{T}{m} + \left(\frac{n\pi}{\ell}\right)^4 \frac{EI}{m}} \tag{2}$$

where T is the axial tensile load. If $T = 0$, the NF is that of a simply supported beam. If $EI = 0$, the equation is that of a flexible taut string where the tension will act as to stiffen the beam, thereby increasing its NF. By making the substitution $T = -N$, and introducing an axial compressive load in place of the axial tensile load, Equation 1 is obtained, and is referred to in the literature as the *"compression-softening"* effect. In the case of axial tension it is known as the *"tension-stiffening"* effect, and is analogous to the so-called *"centrifugal-stiffening"* effect seen with rotating wind turbine blades.

Figure 1a shows the percentage change in NF with increasing axial load according to Equation 1. The magnitude of the externally applied axial force is increased in values of 10% of its Euler buckling load, P_{cr}, up to P_{cr}, for the first three natural bending modes (n) of the beam. A decrease in NFs is observed. In the case where $n = 1$ and $N = P_{cr}$, the NF drops to zero. This is a special case of Equation 1, i.e. $\omega_n = 0$ for $n = 1$ and $N = P_{cr} = \frac{\pi^2 EI}{\ell^2}$. The beam is deemed to have already buckled in its first mode shape and therefore, according to Equation 1 is already deemed to be *'vibrating'* in its first mode at a frequency of $0Hz$. As pointed out in [10], Equation 1 can be written in a dimensionless form;

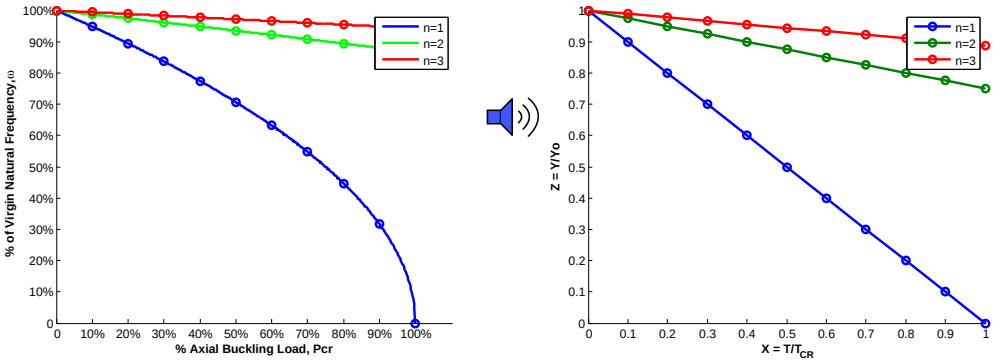

(a) Change in bending freq. with increasing axial compressive force

(b) Sensitivity of change in square of frequency to increasing axial load index

Figure 1: Graphical representation of the *"compression softening"* effect

$$Z = 1 - \frac{1}{n^2}X \tag{3}$$

where Z is an index showing the sensitivity of the square of the frequency to changes in the axial load index. $Z = Y/Y_o$, where $Y = [\omega_n^2/(EI/mL^4)]$ and $Y_o = (n\pi)^4$. The parameter X is the ratio of the axial load to the buckling load and is given by; $X = [N/(\pi^2 EI/L_e^2)]$. This indicates that the sensitivity of the change in frequency with axial load decreases significantly for higher modes of vibration [10], which is represented graphically in Figure 1b.

Many authors [4, 16, 17, 18] argue that the application of the *"compression-softening"* effect to a PSC beam is erroneous from the outset, for a number of different reasons. It has been argued that a prestressing force should be considered as an internal force within the system and is not equivalent to an externally applied axial load [4]. Deák [17] argues Equation 1 is applicable only to an *"external axial compressive force that maintains its original line of action during the vibration of the member, thus being converted into an eccentric force with respect to the axis of the beam."* In essence, the arguments seem to point in the direction that a prestressing force should not be considered to cause the beam to buckle in accordance with Euler buckling theory and therefore Equation 1 is not applicable.

3. Experimental Set-Up

3.1. Dynamic Testing

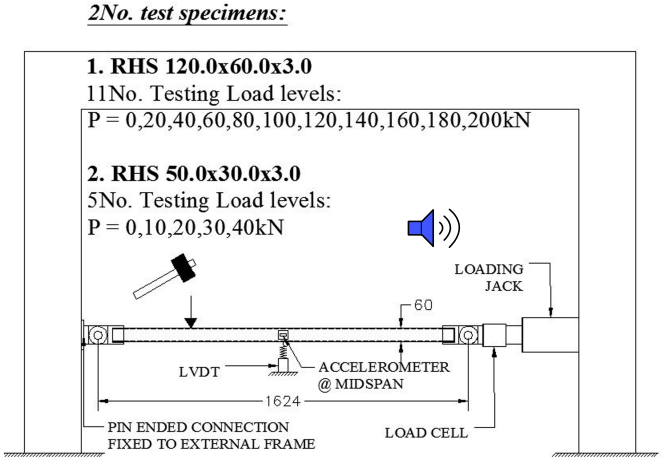

Figure 2: Case 1; External axial load case.

Dynamic impact hammer testing was conducted on 4No. grade S235 steel RHSs, with a Youngs Modulus of 205GPa. The properties of the steel sections are outlined in Table 1 and Table 2. Figure 2 shows the external axial load case (case 1), where dynamic impact hammer testing was carried out on 2No. specimens, a RHS $50 \times 30 \times 3$ (beam 1) and a RHS $120 \times 60 \times 3$ (beam 2), respectively. Each section had a different slenderness ratio, as outlined in Table 2. The purpose of varying the slenderness ratio was to test the validity of Equation 1 for slender members, which are expected to fail, in compression, close to an Euler buckling condition, and stocky members, which show deviation from classical Euler buckling theory.

Since Equation 1 is consistent with Euler buckling theory, it was expected that the dynamic results for the stocky section would deviate from the *compression softening* theory. The test specimen was placed in the small test frame and inserted into two pinned connection joints. One pin was fixed directly to the frame. The other was attached to a load cell, which was in turn connected to a 300 ton loading jack. The jack was mounted on the other side of the frame, as shown in Figure 2. A hydraulic hand pump was connected to the loading jack to vary the external axial load. Impact hammer testing was conducted on the 2No. test specimens at different axial load levels until failure had occurred.

Table 1: Properties of steel RHS sections tested

Property	**RHS** $50 \times 30 \times 3$	**RHS** $120 \times 60 \times 3$
Beam #	Beam 1	Beam 2
m (kg/m)	3.41	8.12
A (cm^2)	4.34	10.30
I_{zz} (cm^4)	5.94	65.50

Table 2: Properties of experimental cases

	Case 1	**Case 2**
Figure #	Figure 2	Figure 3
Span, ℓ (m)	1.624	1.500
Slenderness Beam 1, λ_{zz_1}	139	128
Slenderness Beam 2, λ_{zz_2}	64	59
Beam 1, ω_{1_1} (Hz)	36.0	42.2
Beam 2, ω_{1_2} (Hz)	77.5	90.9

Figure 3 shows the post-tensioned load case (case 2) where impact hammer testing was carried out on the same RHSs. The sections were post-tensioned using a 15.7mm Freysinnet 7 wire concentric strand. The strand was anchored with the appropriate collets either side of 2No. 300 ton loading jacks. A load cell and a baseplate were positioned between the jack and the end of the steel RHS section, helping to evenly transfer the post-tensioning load into the section. 2No. jacks and 2No. load cells were used in order to balance the mass under vibration. Multiple load cells ensured an even distribution of post-tensioning load throughout the length of the section. The post-tensioned section was supported on either side by knife-edge supports that were a distance of 1.500m apart. One of the jacks was connected to a hydraulic hand pump to transfer a post-tensioning load into the section.

The Multiple Input, Multiple Output (MIMO) method of dynamic impact testing was implemented, in which there were multiple dynamic excitation points and multiple instrumentation response points. 5No. equally spaced

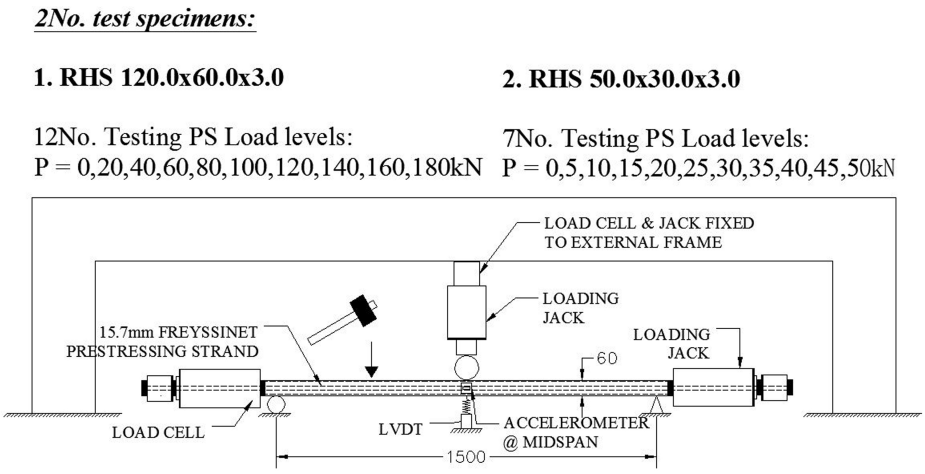

Figure 3: Case 2; post-tensioned load case

input locations were used as both input points and response points as shown in Figure 4. Strain gauges were placed at each of the response points, labelled L1-L5, and an accelerometer was mounted at mid-span on each section, at location L3. 10No. strikes of the sledge hammer were applied at each input point for each load increment, for repeatability, giving a total of 50 frequency data points per axial load level.

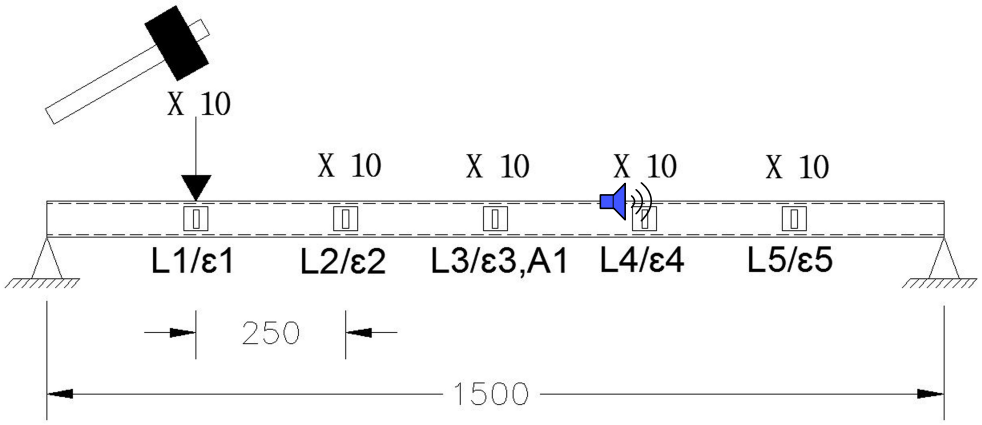

Figure 4: Instrumentation of steel specimens

3.2. Static Testing

Static 3 point bending tests were ~~also~~ conducted on both beam 1 and beam 2 for the post-tensioned load case (beam 1, case 2 and beam 2, case 2). The apparatus was set up as outlined in Figure 3 and Figure 4. The beams were supported at a span distance of 1.500m by two knife-edge supports in the form of equal angle sections. Jacks were placed on either end of the respective beams and a 15.7mm diameter Freyssinet post-tensioning strand was threaded through the hollow in the respective RHS beams. The post-tensioning load level was increased, and at each load increment, a point load was applied at midspan by an external reaction frame (Figure 3). The corresponding deflection was measured using an LVDT placed at midspan. The load-deflection relationship enabled the static flexural rigidity of the beams to be calculated at each post-tension load increment using the following deflection equation for a simply supported beam, with a point load at midspan;

$$\delta = \frac{P\ell^3}{48EI} \tag{4}$$

where δ is the midspan deflection of the beam, P is the magnitude of the midspan point load, ℓ is the span length between supports, E is the Young's Modulus of elasticity of the material (in this case S235 steel), and I is the second moment of area of the beam about the axis of bending. Rearranging Equation 4 allows the effective static flexural rigidity, EI_{eff} to be calculated;

$$EI_{eff} = \frac{P\ell^3}{48\delta} \tag{5}$$

The corresponding static-equivalent prediction for the n^{th} natural frequency of the post-tensioned RHS section is then given as;

$$\omega_n = \left(\frac{n\pi}{\ell}\right)^2 \sqrt{\frac{EI_{eff}}{m}} \tag{6}$$

This has been compared to the values that were obtained dynamically and the results are given in Section 5.1.

4. Experimental Analysis

4.1. Calculation of Fundamental Natural Frequency, ω_1

Following collection of the impact hammer data, the raw signal (acceleration-time data) was imported into MATLAB [25]. The Fast Fourier Transform (FFT) was then performed on the acceleration data in the time domain in order to represent the signal in the frequency domain. A peak picking algorithm was then used to identify the peaks in the frequency domain.

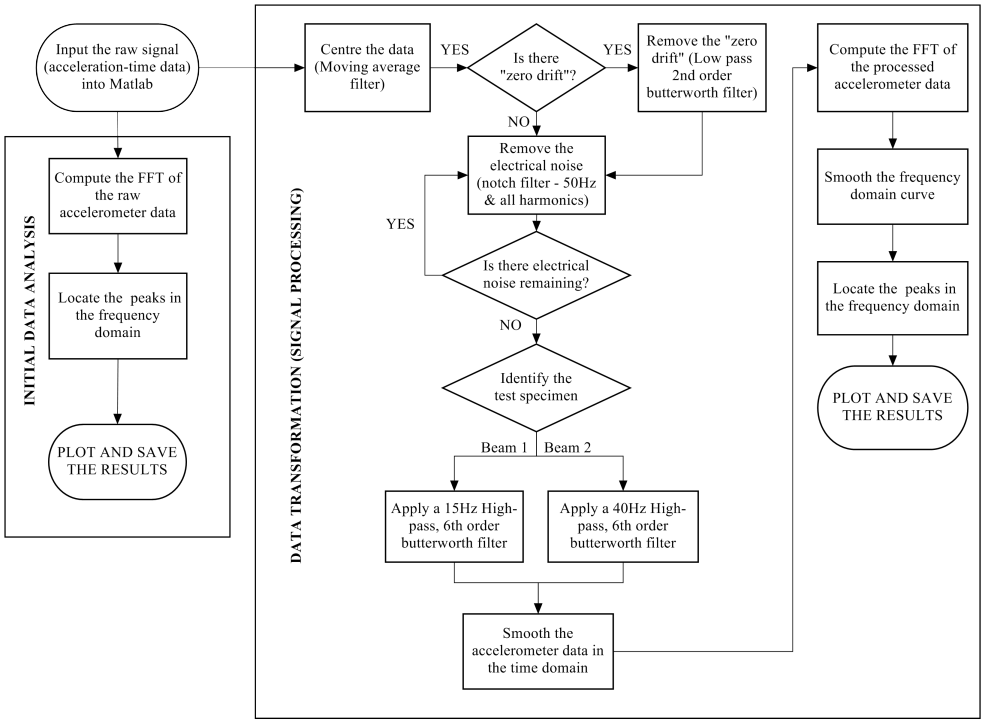

Figure 5: Signal Processing Procedure

The raw signal contained significant electrical noise. In some cases, a zero drift in the accelerometer was observed. Subsequently, the peaks in the frequency domain were initially difficult to determine. A signal processing algorithm was developed in MATLAB [25] and is outlined in Figure 5. The signals were processed to eliminate noise and remove the zero drift. The processed acceleration data was then smoothed in the time domain and the FFT was recomputed. Finally, the data was smoothed in the frequency domain. Following smoothing in the frequency domain, the peak picking

algorithm was re-~~invoked~~ and the peaks were again determined. The search bands for the fundamental frequency of each beam were defined as 15-45Hz for Beam 1 and 60-85Hz for Beam 2. The raw data and the processed data were compared, and following processing, the structural peaks were much easier to identify. The peaks in the frequency domain were identified as the natural frequencies of the structural system. This algorithm is required to deal with the high levels of noise associated with impact hammer testing of these types of metallic sections.

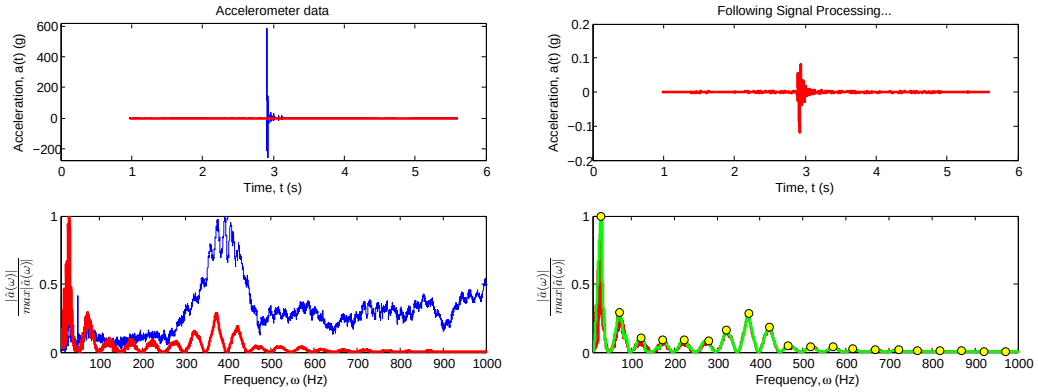

(a) Raw (blue) vs. processed (red) data (b) Identif. of NFs of Beam 1 Case 1

Figure 6: Signal processing and peak identification; Beam 1 Case 1

Figures 6-9 show typical accelerometer response for each beam and case combination. Figures 6a-9a show the accelerometer signals in both the time and frequency domain, before the signal was processed to eliminate noise (blue) and after signal processing (red). The natural vibration frequencies of the respective structural systems are identified as the peaks in the frequency domain. The peaks are initially difficult to determine in the unfiltered (blue) signals, however, following processing (red) the peaks become readily identifiable. The zero drift in the signal has been removed, along with the 50Hz electrical noise and all of its harmonics, using a high-order notch (bandpass) filter. Finally, a high pass filter is invoked, removing all low frequency noise, below the expected first natural frequency peak.

Figures 6b-9b show the processed signal in both the time and the frequency domain. The scale of the acceleration axis in the time domain of each signal is significantly reduced from Figures 6a-9a to Figures 6b-9b, indicating the extent of of the amplitude attributable to noise components.

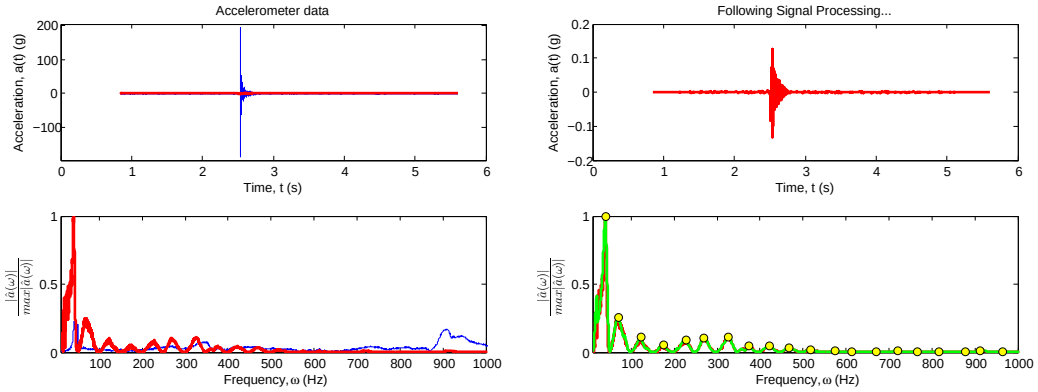

(a) Raw (blue) vs. processed (red) data (b) Identif. of NFs of Beam 1 Case 2

Figure 7: Signal processing and peak identification; Beam 1 Case 2

For the Figures shown, the reduction in amplitude is between $\times 500$, for Figure 8 and $\times 2250$, for Figure 6. The peaks are identified in Figures 6b-9b as the yellow points. The first 20 peaks in the range of 0-1000Hz have been identified.

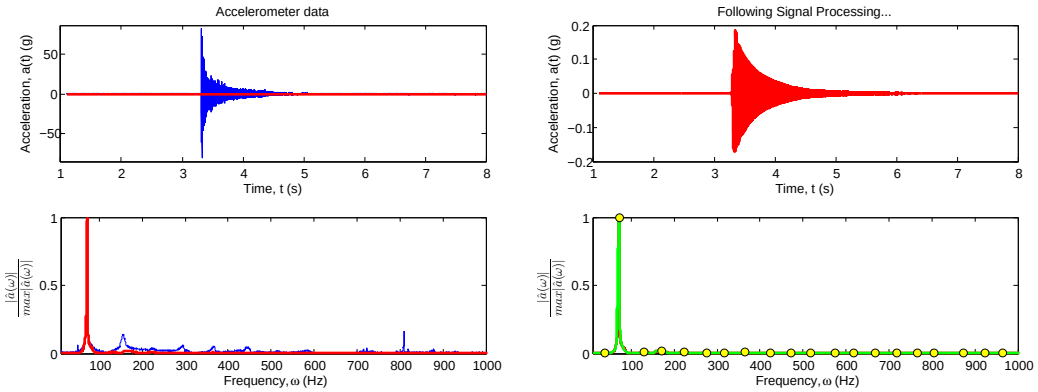

(a) Raw (blue) vs. processed (red) data (b) Identif. of NFs of Beam 2 Case 1

Figure 8: Signal processing and peak identification; Beam 2 Case 1

4.2. Calculation of Damping Ratio, ξ

The damping ratio, ξ of the beams were calculated for each axial load level using the half-power bandwidth method, ~~as outlined by~~ Clough & Pen-

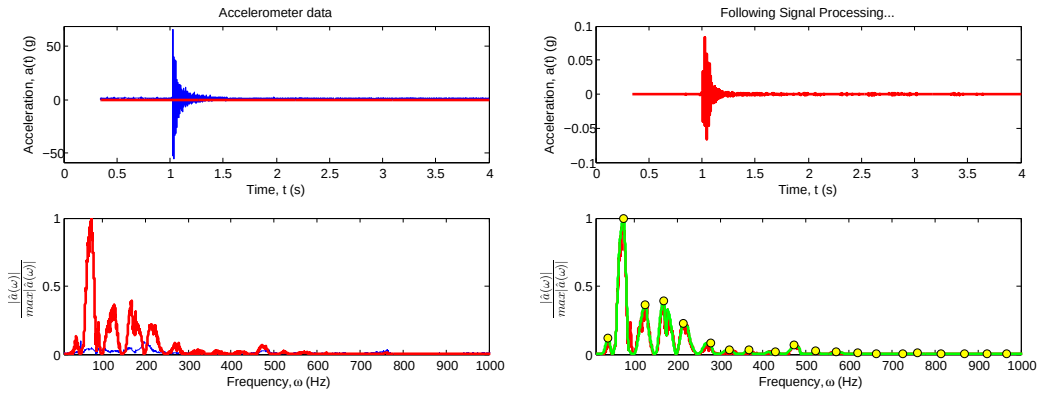

(a) Raw (blue) vs. processed (red) data (b) Identif. of NFs of Beam 2 Case 2

Figure 9: Signal processing and peak identification; Beam 2 Case 2

zien [26], Chopra [27] and Wu [28]. As outlined by Wu [28], the half-power bandwidth method enables evaluation of damping from forced vibration tests without knowing the applied force, and is thus used in vibration and modal testing. By assuming that the damping ratio ξ is small and that the frequency at maximum amplitude is approximately equal to the undamped fundamental frequency ω_1, the classical result relating the damping ratio to the half-power bandwidth can be written as;

$$\xi = \frac{\omega_b - \omega_a}{2\omega_1} \tag{7}$$

where ω_a and ω_b are the half-power frequencies (i.e. the frequencies of the function at Max. Amplitude/$\sqrt{2}$). As pointed out by Wu [28], the classical result is only valid for damping ratio less than 0.1, and is not a good prediction for $\xi > 0.1$.

An example of the calculation of the damping ratio in accordance by the half-power bandwidth method is shown in Figure 10.

5. Experimental Results

Both the fundamental frequencies, ω_1 and the respective damping ratios ξ have been calculated for increasing axial load levels, and the results are presented in this section. The fundamental frequencies have been identified as the main peak in the expected range. The damping ratios have been

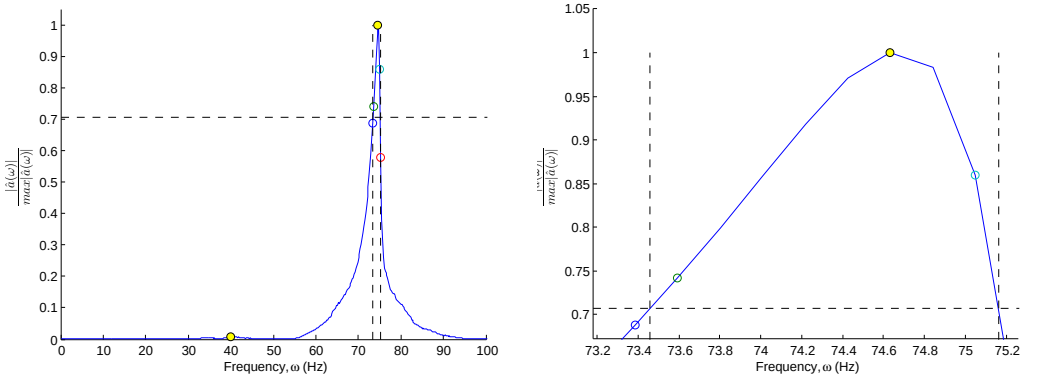

(a) (b)

Figure 10: Half-power bandwidth method of calculation of damping ratio, ξ

calculated in accordance with the half-power bandwidth method.

5.1. Fundamental Bending Frequencies, ω_1

Figure 11 shows the peaks in the frequency domain for each axial load level and for each impact hammer test conducted. There are 50 iterations of the impact response signals at each axial load level. The relative modal amplitude is displayed on the vertical axis, while the horizontal plane consists of the frequency axis (Hz) and the axial load level (kN). The size of the data point is directly related to the relative modal amplitude. The modal amplitude has been normalised by dividing by its maximum value, expressed as $\frac{\hat{a}(\omega)}{max(\hat{a}(\omega))}$. The relative participation of each mode to the overall dynamic response of the beams can be compared in these graphs. For example, for both post-tensioned beams (beam 1, case 2, Figure 11b & beam 2, case 2, Figure 11d) it can be seen that the overall response of the beam is quite complex and contains a significant proportion due to many modes. In comparison, for the externally axially load case (beam 1, case 1, Figure 11a & beam 2, case 1, Figure 11c), the dominance of the first mode is more readily identifiable. This is exceptionally clear for beam 2, case 1 in Figure 11c, where the dominance of the first mode of vibration is evident.

Comparing Figure 11 to Figure 12 leads to an interesting observation. When the total response of the structural system is complex, with components that can be attributed to many different modes, as can be seen in Figures 11b and 11d, and to a lesser extent, Figure 11a, the scatter in

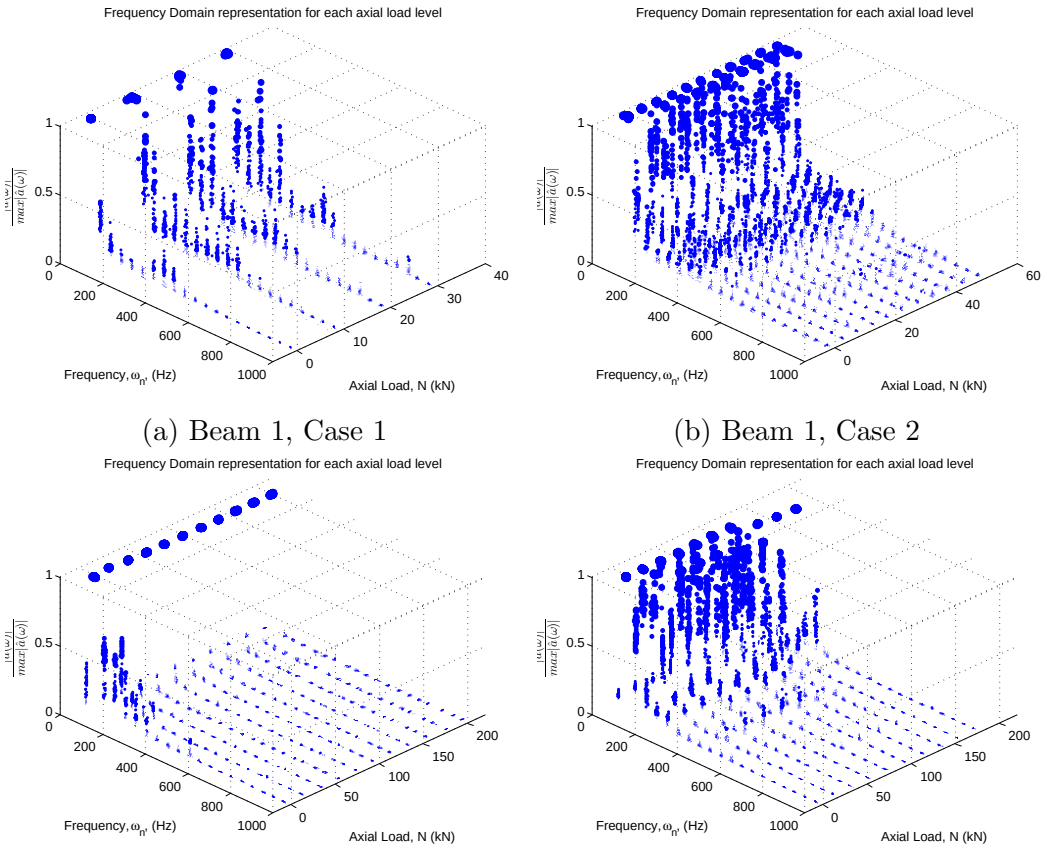

(a) Beam 1, Case 1

(b) Beam 1, Case 2

(c) Beam 2, Case 1

(d) Beam 2, Case 2

Figure 11: Graph of peaks in frequency, load and relative modal amplitude, 3D-space

the prediction of the first natural frequency is very high, as can be seen in Figures 12b, 12d and 12a and indicated by the standard deviation in the data. However, in the case where the response of the structural system is significantly dominated by the fundamental frequency, as in Figure 11c, the standard deviation is significantly decreased and the prediction of the first natural frequency is very precise, with an extremely low standard deviation, as shown in Figure 12c. It should be noted that for lower values of axial load, the response is slightly more complex for Beam 2, Case 1 (Figure 12c), with many modes contributing to the response. Consequently, we see a much higher scatter in the prediction of the fundamental frequency and a smaller

standard deviation.

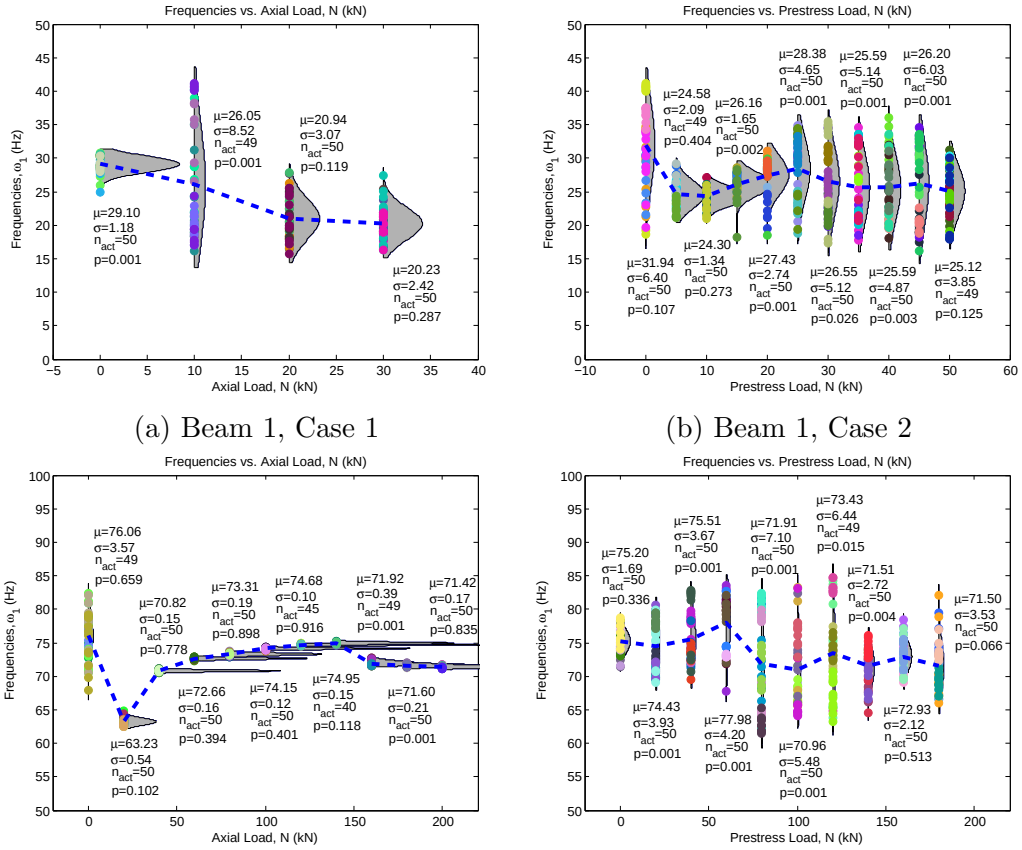

(a) Beam 1, Case 1

(b) Beam 1, Case 2

(c) Beam 2, Case 1

(d) Beam 2, Case 2

Figure 12: Observed changes in ω_1 with N for different steel beams

In order to analyse the significance of the changes observed in the estimation of the natural frequency of the sections with increasing axial load, a linear regression analysis was applied to each beam and load case combination. The results are presented in Appendix A, Figure A.1 in conjunction with Table A.1. It should be pointed out to begin with that the purpose of this regression analysis is not for interpolation, extrapolation or prediction of any values of fundamental frequency based on axial load level, but rather as a tool to analyse the statistical significance of the changes observed in the data. Table A.1 shows the regression parameters and the results of statistical t-tests charting whether the linear regression intercept and slope parameters

are statistically significantly different from zero or not for each beam and load case combination. A significance level of $\alpha = 0.05$ has been chosen for the tests. In each beam/load case combination a statistically significant change in fundamental frequency with increasing axial load level has been observed. For beam 1, case 1, a statistically significant decreasing trend is observed, indicating that the natural frequency of an externally axially loaded slender steel section will decrease with increasing external axial load. For beam 1, case 2, a statistically significant decreasing trend is again observed, however the rate of change (magnitude of the regression slope parameter) is not as large as that for beam 1, case 1. This indicates that the rate of change of frequency with increasing axial load level is different for an external axial load (case 1) than it is for the post-tensioned load case (case 2). This can be seen clearly in Figure 13.

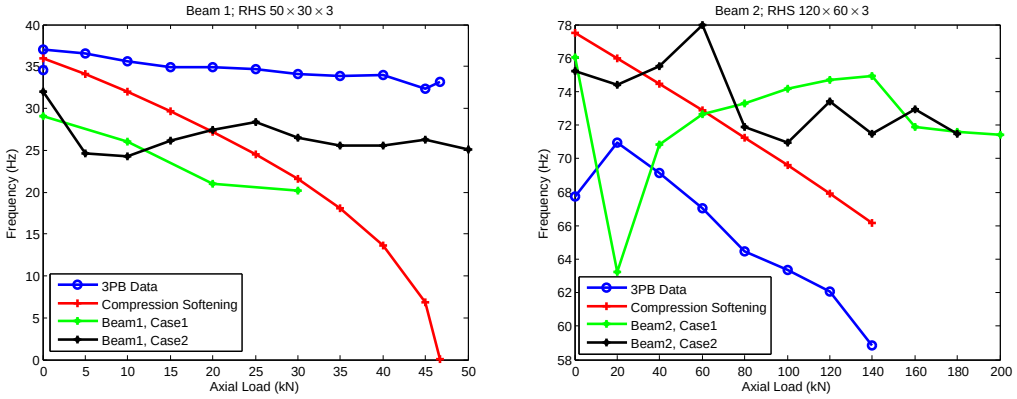

(a) Beam 1, Case 1 (b) Beam 1, Case 2

Figure 13: Means of dynamic test results plotted with static 3 point bending data and Equation 1

For beam 2, case 1 a statistically significant increasing trend is observed, indicating that for an externally axially loaded stocky section, the natural bending frequency increases with increasing external axial force. However, it is questionable whether a linear fit is correct in this case, as, from Figure 12c and A.1c, a non-linear second order, or possibly an asymptotic trend is identifiable. For beam 2, case 2, again a statistically significant decreasing trend in natural bending frequency with increasing axial load level is observed, however the magnitude of the regression slope parameter is less than for both beam 1 - load case combinations.

Figure 13 compares the prediction of the change in fundamental bending frequency of the beam sections according to *"compression-softening"* theory (Equation 1) (red) to the means of the dynamic results for the external axial load case (load case 1 - green), the post-tensioned load case (load case 2 - black), and the results of the static-equivalent frequency of the post-tensioned load case (load case 2 - blue). Figure 13a shows the results for beam 1, RHS $50 \times 30 \times 3$, with a slenderness ratio of between 128 and 139, depending on the load case, as outlined in Table 2. It can be seen from Figure 13a that the external axial load case shows some good agreement in terms of the decreasing trend in fundamental bending frequency with increasing external axial load. The green line and the red line are almost parallel. The frequency of the external axial load case has been shifted down however, and this may be attributed to lack of ideal conditions. The entire structural system consists of a frame and loading jack, which would act as to lower the bending frequencies. Buckling was reported at an external axial load of 40kN. The predicted failure load in accordance with EC3 is 35.4kN. Buckling occurred when the section was loaded axially to 40kN and the beam was struck laterally with the impact hammer during dynamic testing. As a result, it was impossible to obtain an estimation of the natural frequency at this load level. However, the trend is still observable up to this point. The black line indicates the change in the mean of the frequencies due to an increasing post-tensioning load, that is induced in the section by the way of a post-tensioning strand threaded through the beam hollow and jacking against either end of the beam to elongate the strand. It can be seen from Figure 13a that the post-tension load case (case 2) does not follow the same trend as either the external axial load case (green) or that predicted by *"compression-softening"* theory (Equation 1). However, it does follow a very similar trend to the static prediction of the frequency due to 3-point bending tests, as described in Section 3.2. A downwards shift to the dynamic measurement of the fundamental frequency is again observable. It can be concluded that, for slender sections, that are expected to behave in good agreement with Euler buckling theory, that *"compression-softening"* is indeed valid for externally axially loaded members. However, Equation 1 is not applicable to post-tensioned structures. In this case, a slight decreasing trend in the fundamental frequency is observable, however it is not of the same rate as predicted by Equation 1. It can be concluded, that for slender member, a post-tensioned load is not dynamically equivalent to an external axial load. Figure 13b, shows the results for beam 2, RHS $120 \times 60 \times 3$. It has a slenderness ratio of approximately 60, as outlined in Table 2, and, accord-

ing to code-based approaches, such as Eurocode 3 (EC3) [29], is expected to deviate from Euler buckling theory as a result. It can be seen that both the external axial load case (green) and the post-tensioned load case (black) deviate greatly from the trend expected in accordance with Equation 1. The static 3-point bending prediction of the frequency follows a similar decreasing trend, as predicted by Equation 1, however, an initial increase is observed, with seating load, as in Figure 13a. There is also a downward shift in the 3-point bending prediction of the frequency from Equation 1, which again can be attributed to the lack of ideal conditions, and the effect of the weight of the jacks on the beam response. In summary, it can be concluded that stocky sections, with low and medium slenderness ratios do not follow the trend predicted by *"compression-softening"* theory, neither for the external axial load case (load case 1) or for the post-tensioned load case (load case 2). It was found, as expected that *"compression-softening"* is only valid for externally axially loaded slender members (with a slenderness ratio greater than approximately 120) that behave in accordance with Euler buckling theory.

Figure A.2, Appendix A, shows a Normal probability paper for the measured values of the fundamental frequencies of each of the four beam and load case combinations. From visual inspection of the plots, it may be considered that both post-tensioned load cases (Figures A.2b and A.2d) are in fact visually consistent with what would be expected from data Normality, including the deviation in the tails of the plot, i.e. the extreme values. Data normality must be rejected for both external axial load cases (Figures A.2a and A.2c).

5.2. Damping Ratio, ξ

In this section, the results relating to the calculation of the damping ratio are discussed. The damping ratio, ξ, was calculated from the half-power bandwidth method, as outlined in Section 4.2. Figure 14 shows the calculated values of the damping ratio at each axial load level, for each of the four beam and load cases. In most cases, the estimated damping ratios are found to have been in the expected range of $0-5\%$ damping, however, there are some large overestimations of the damping ratio, especially for beam 1, case 2 (Figure 14b), where, especially for zero post-tensioning force, extreme overestimation of the damping is reported, e.g. some estimations of $\xi > 60\%$. This inaccuracy may be attributed to the relative mass of the jacks on either end of the beam in comparison to the mass of the beam itself, and

the contribution of the vibration of the jacks to the overall vibration of the structural system, leading to extreme overestimation of the damping ratio. As pointed out by Wu [28], the half-power bandwidth method is only valid for $0 < \xi < 0.1$ and all data outside of this range must be considered as outliers.

In all beam and load case combinations, a general decreasing trend in damping ratio, ξ with increasing axial load level, N is observable. Again, as with Figure 12c, Figure 14c displays a very precise measurement of ξ for an external axial load of 20kN upwards. This is attributed to the fact that the structural response of the beam was dominated by the fundamental bending mode, as is observable in Figure 11, specifically in Figure 11c.

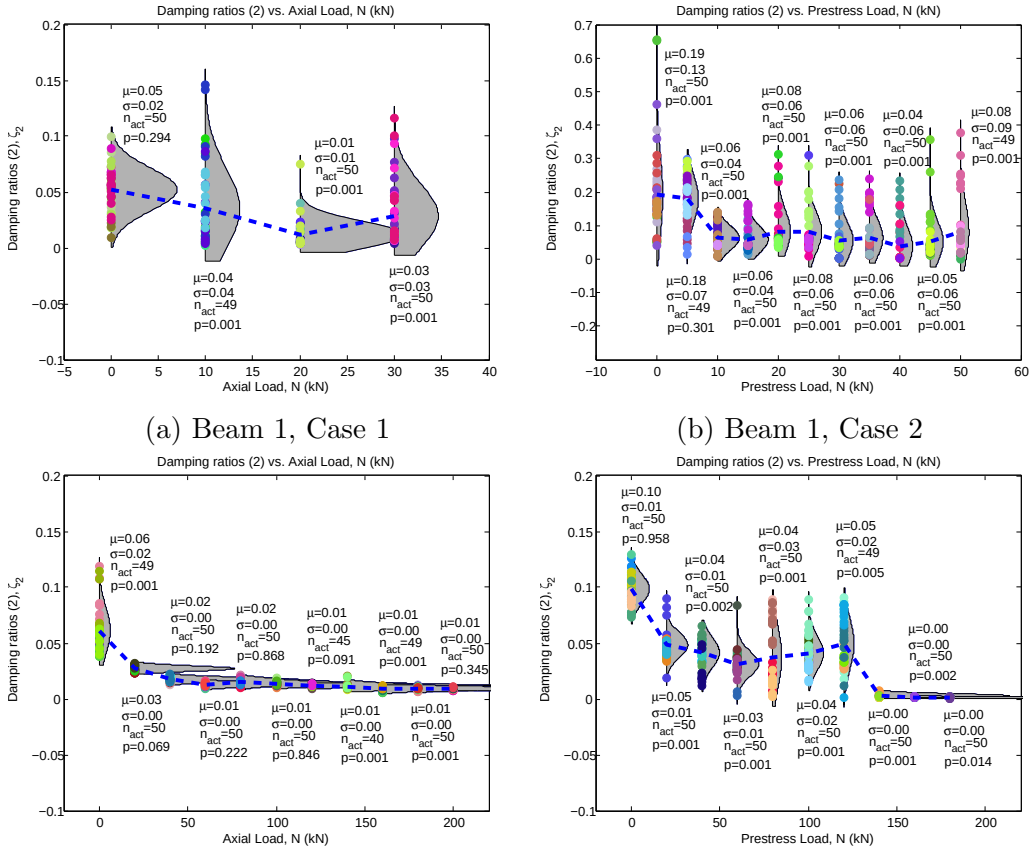

(a) Beam 1, Case 1

(b) Beam 1, Case 2

(c) Beam 2, Case 1

(d) Beam 2, Case 2

Figure 14: Observed changes in ξ with N for different steel beams

Figure A.3 shows a linear regression analysis by regressing the measured damping ratio, ξ on the axial load level, N. When analysed in conjunction with Table A.2, this indicates that there is a statistically significant decreasing trend in estimation of the damping ratio with increasing axial load level. Figure A.4 shows the Normal Probability Papers of the measured damping ratio for each of the four beam and load case combinations. Using the visual method, normality must be rejected for all four beam and load cases

5.3. Beam Failure Conditions

Table 3: Failure conditions of RHS sections

Property	**RHS** $50 \times 30 \times 3$	**RHS** $120 \times 60 \times 3$
Beam #	Beam 1	Beam 2
$N_{b,Rd_{yy}}$ (kN)	35.4	187.5
$P_{CR_{yy}}$ (kN)	46.7	514.7
$N_{c,Rd}$ (kN)	97.1	230.5
Failure Reported (kN)	40	260

The failure conditions for each of the four beam and load case combinations were very different. Table 3 charts the failure load of the external axially loaded sections, and compares the values to what is predicted in accordance with EC3 [29] ($N_{b,Rd_{yy}}$), what is predicted from Euler buckling theory ($P_{CR_{yy}}$) and what is predicted from crushing of the member, in accordance with EC3 [29] ($N_{c,Rd}$). Figure 15 shows the beam failure conditions in the laboratory. The slender section, beam 1 - RHS $50 \times 30 \times 3$, as shown in Figure 15a, failed in a manner consistent with what is predicted by Euler buckling theory at a load of 40 kN, which is 11.5% greater than the EC3 design load of 35.4kN, and 14% less than the critical load predicted by Euler buckling theory. The stocky section, beam 2 - RHS $120 \times 60 \times 3$, as shown in Figure 15a, failed in a local manner, close to the support at a value of 260kN. Interestingly, this value is approximately 13% greater than the design crushing load in accordance with EC3 [29]. However, as expected, for a stocky section, it is well below (approx. 45%) of the predicted Euler buckling critical load of 514.7kN.

No failure condition was reached for the slender post-tensioned section (i.e. beam 1, case 2). In the case of the post-tensioned stocky section, a

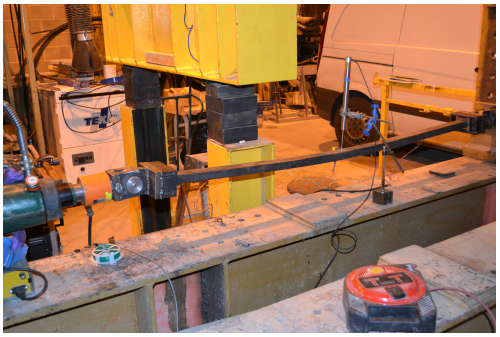

(a) Beam 1, Case 1; Failure reported at 40kN

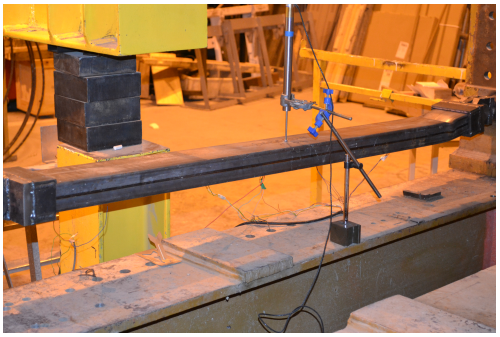

(b) Beam 2, Case 1; Failure reported at 260kN

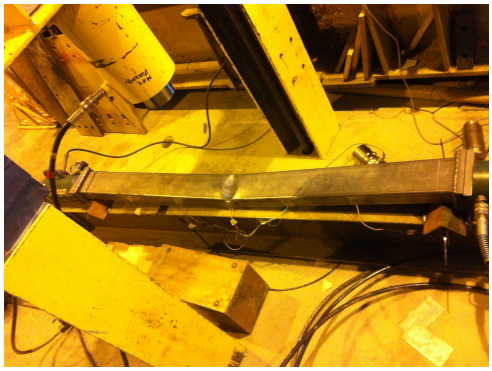

(c) Beam 2 Case 2; Failure reported at 160kN PT load & 6kN PL

Figure 15: Failure conditions of RHS sections

plastic hinge formed at midspan at an axial load of 140kN, combined with a midspan point load of 6kN. This can be seen in Figure 15c. The section, in accordance with EC3 [29], is designed to resist a midspan point load of 12.42kN, therefore, at a post-tension load of 140kN, a 50% reduction in load carrying capacity was observed.

6. Summary & Conclusions

The above results have been obtained after gathering and analysing 1750 different dynamic response measurements, including the cases of slender and stocky sections that have been both post-tensioned and externally axially loaded. The volume of data collected enabled a statistical analysis of the

results for a combination of beam and load cases to be conducted. The main conclusions derived from this broad study are as follows;

1. An externally axially loaded slender section displays good agreement with the *"compression-softening"* effect, as the obtained results have shown. A post-tensioned slender section deviates from what is expected from *"compression-softening"* theory, however, does display a decreasing trend in fundamental bending frequency, ω_1 with increasing post-tensioning load.

2. An externally axially loaded stocky section does not follow the trend predicted by *"compression-softening"* theory. A statistically significant increasing trend in ω_1 is observed with increasing axial load level. A post-tensioned stocky section also deviates from *"compression-softening"* theory, however a statistically significant decreasing trend was observed.

3. Post-tension load is phenomenologically different to an external axial load and is not equivalent to an external axial load.

4. A post-tensioning load does not cause Euler buckling to occur.

5. *"Compression-softening"* is not valid for pre- or post-tensioned structures, therefore the use of Equation 1 is erroneous for post-tensioned concrete structures.

6. In all cases, a decrease in damping ratio, ξ is observed with increasing axial load level.

7. The precision of prediction of the fundamental frequency is related to the complexity of dynamic response of the signal, and the proportion of dynamic response attributed to the fundamental mode.

The main implications of the results are that the *"compression-softening"* equation must be eliminated from discussion of all forms of post-tensioned structures, as the effect of an external axial load and a post-tensioning load on the dynamics of post-tensioned structures are different on a phenomenological level.

Further research is required to determine exactly how the fundamental frequency of pre- and post-tensioned concrete structures changes with increasing post-tensioning force, however, based on the above results, the fundamental frequency of pre- and post-tensioned concrete structures are not predicted to behave in accordance with *"compression-softening"* theory.

Acknowledgements

The authors would like to gratefully acknowledge the financial support donated by the Irish Research Council (IRC) under its Embark initiative. The authors would also like to sincerely thank Banagher Concrete, Heitons Steel, Roadstone Ireland, Fairyhouse Steel, and Freyssinet Ireland for their support in supplying testing materials throughout the duration of the project to date.

Appendix A.

The statistical significance of the regression slope and intercept parameters for regressing both fundamental bending frequencies, ω_1 and Damping Ratios, ξ on applied axial load for all beam and load case combinations are given in Table A.1 and Table A.2. Statistical t-tests have been carried out to determine if the regression slope and intercept parameters are statistically significantly different from zero, or not.

Linear regression lines have been fitted to the data and the results are observed in Figures A.1 and A.3. The Normality of both the fundamental bending frequency and the damping ratios have been tested by plotting the results on a Normal Probability Paper, and the results are displayed in Figures A.2 and A.4.

Appendix A.1. Fundamental Bending Frequencies, ω_1

Table A.1 shows the calculated linear regression intercept parameter (α_0), and slope parameter (α_1) when regressing ω_1 on N for all four permutations of beam and load cases. The corresponding linear regression equations are obtained by substituting into the following formula;

$$\omega_1 = \alpha_0 + \alpha_1 N \tag{A.1}$$

Table A.1: Statistical analysis on regression parameters for ω_1 on N

B/C	Reg. P.	Value	SE	t-value	t-crit.	p	95% CI
B1 C1	$\alpha_{0,11}$	28.7612	0.5574	51.5969	1.9720	0.0000	(27.6620,29.8605)
	$\alpha_{1,11}$	-0.3236	0.0308	-10.5204	1.9720	0.0000	(-0.3842,-0.2629)
B1 C2	$\alpha_{0,12}$	27.6906	0.3709	74.6608	1.9643	0.0000	(26.9621,28.4192)
	$\alpha_{1,12}$	-0.0477	0.0130	-3.6845	1.9643	0.0003	(-0.0732,-0.0223)
B2 C1	$\alpha_{0,21}$	71.3579	0.2682	266.0298	1.9644	0.0000	(70.8310,71.8848)
	$\alpha_{1,21}$	0.0084	0.0023	3.5894	1.9644	0.0004	(0.0038,0.0130)
B2 C2	$\alpha_{0,22}$	75.6530	0.3855	196.2659	1.9647	0.0000	(74.8956,76.4103)
	$\alpha_{1,22}$	-0.0239	0.0037	-6.5195	1.9647	0.0000	(-0.0311,-0.0167)

Appendix A.2. Damping Ratios, ξ

Table A.2 shows the calculated linear regression intercept parameter (β_0), and slope parameter (β_1) when regressing ξ_1 on N for all four permutations of beam and load cases. The corresponding linear regression equations are obtained by substituting into the following formula;

$$\xi_1 = \beta_0 + \beta_1 N \tag{A.2}$$

Table A.2: Statistical analysis on regression parameters for ξ_1 on N

B/C	Reg. P.	Value	SE	t-value	t-crit.	p	95% CI
B1 C1	$\beta_{0,11}$	0.0458	0.0032	14.2186	1.9720	0.0000	(0.0395,0.0522)
	$\beta_{1,11}$	-0.0010	0.0002	-5.3699	1.9720	0.0000	(-0.0013,-0.0006)
B1 C2	$\beta_{0,12}$	0.1371	0.0062	22.1801	1.9643	0.0000	(0.1249,0.1492)
	$\beta_{1,12}$	-0.0021	0.0002	-9.8760	1.9643	0.0000	(-0.0026,-0.0017)
B2 C1	$\beta_{0,21}$	0.0344	0.0010	35.8787	1.9644	0.0000	(0.0325,0.0363)
	$\beta_{1,21}$	-0.0002	0.0000	-19.4633	1.9644	0.0004	(-0.0002,-0.0001)
B2 C2	$\beta_{0,22}$	0.0714	0.0017	41.2609	1.9647	0.0000	(0.0680,0.0748)
	$\beta_{1,22}$	-0.0004	0.0000	-24.6953	1.9647	0.0000	(-0.0004,-0.0004)

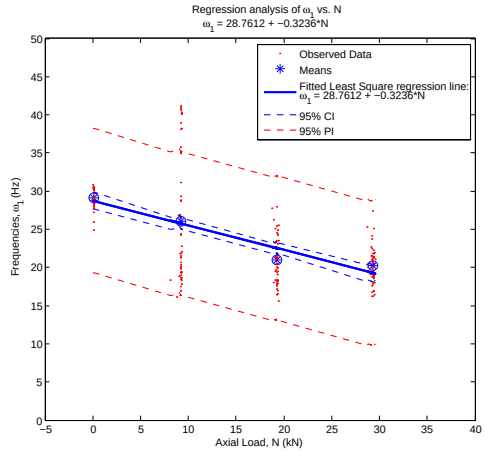

(a) Beam 1, Case 1

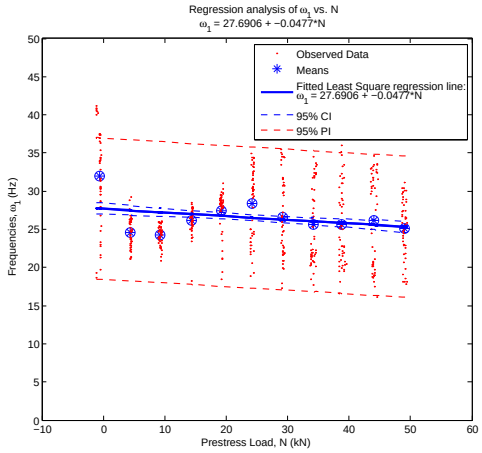

(b) Beam 1, Case 2

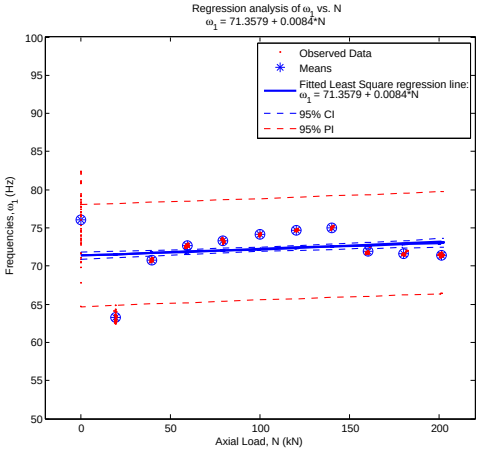

(c) Beam 2, Case 1

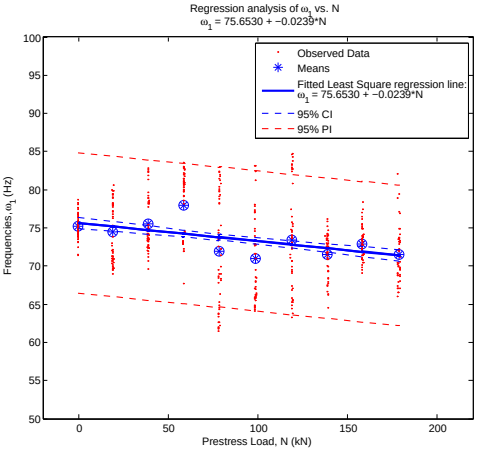

(d) Beam 2, Case 2

Figure A.1: Regression analysis; ω_1 vs. N for different steel beams

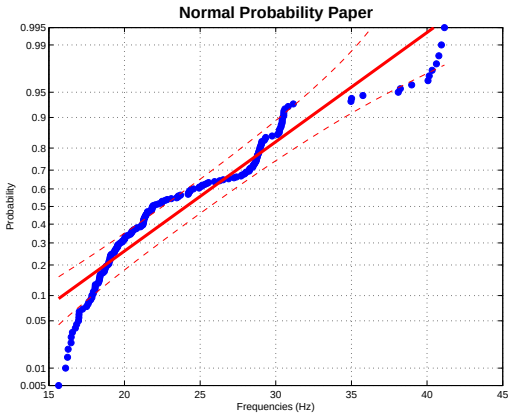

(a) Beam 1, Case 1

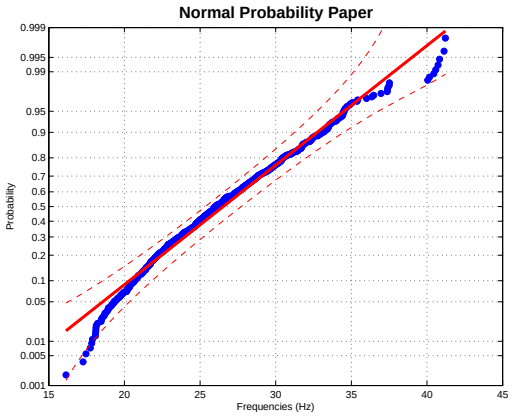

(b) Beam 1, Case 2

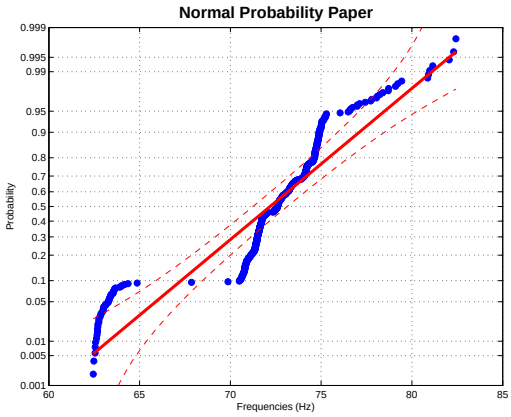

(c) Beam 2, Case 1

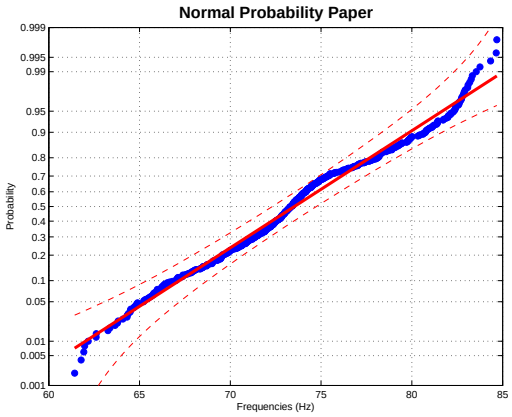

(d) Beam 2, Case 2

Figure A.2: Normal Probability Plots of Fundamental Bending Frequency, ω_1 for each beam/load case combination

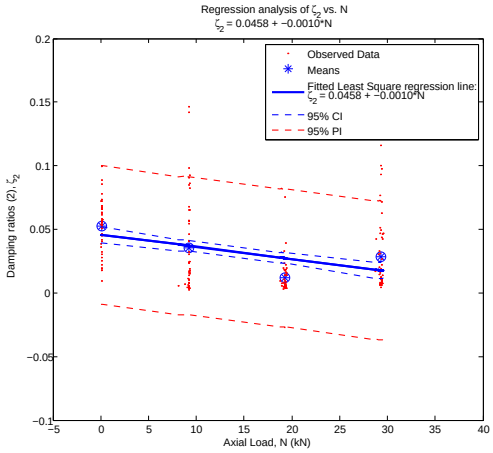

(a) Beam 1, Case 1

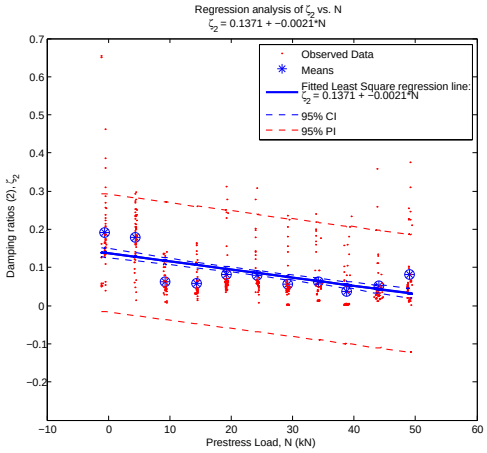

(b) Beam 1, Case 2

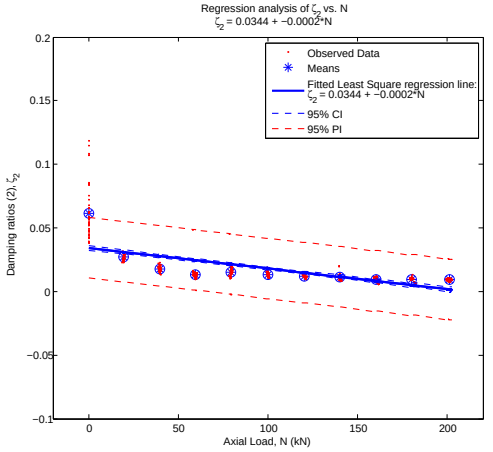

(c) Beam 2, Case 1

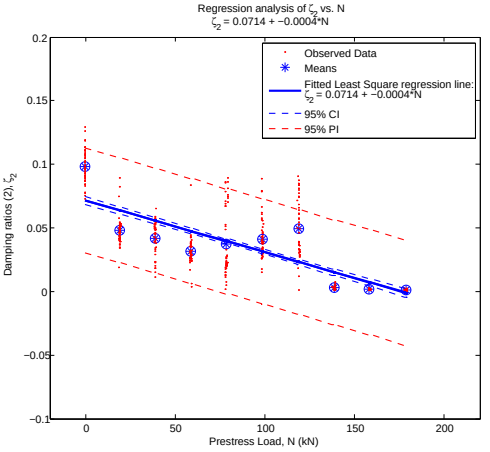

(d) Beam 2, Case 2

Figure A.3: Regression analysis; ξ vs. N for different steel beams

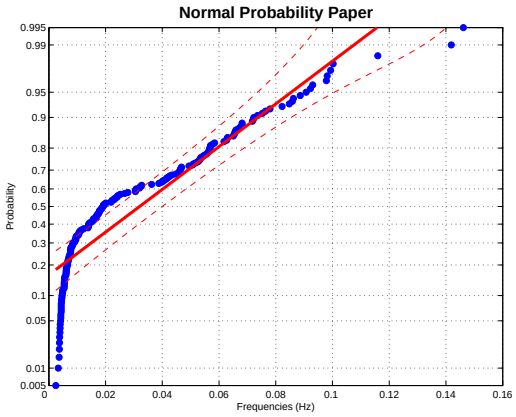

(a) Beam 1, Case 1

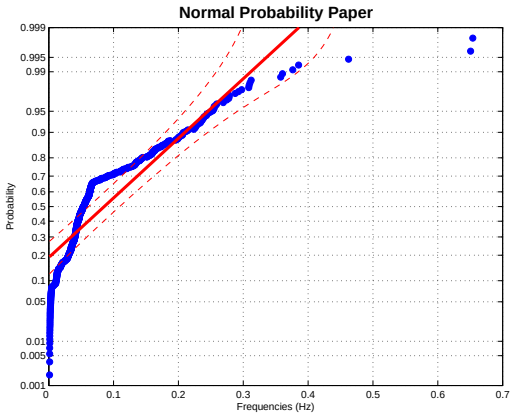

(b) Beam 1, Case 2

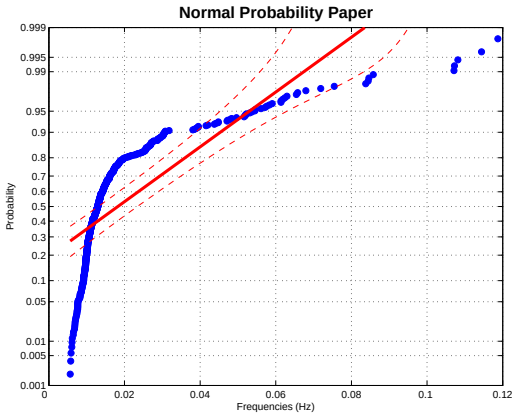

(c) Beam 2, Case 1

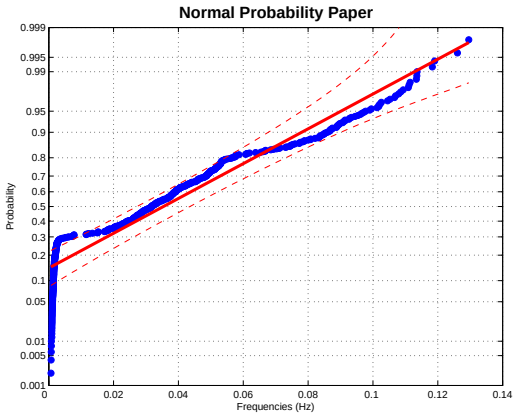

(d) Beam 2, Case 2

Figure A.4: Normal Probability Plots of Damping Ratio, ξ for each beam/load case combination

References

[1] A. Quilligan, A. O'Connor, V. Pakrashi, Fragility analysis of steel and concrete wind turbine towers, Engineering Structures 36 (0) (2012) 270 – 282.

[2] F. Tse, I. Morse, R. Hinkle, Mechanical vibrations: theory and applications, Allyn and Bacon series in mechanical engineering and applied mechanics, Allyn and Bacon, 1978.

[3] K. K. Raju, G. V. Rao, Free vibration behavior of prestressed beams, Journal of Structural Engineering 112 (1986) 433–437.

[4] A. Dall'Asta, G. Leoni, Vibrations of beams prestressed by internal frictionless cables, Journal of Sound and Vibration 222 (1) (1999) 1 – 18.

[5] A. Miyamoto, K. Tei, H. Nakamura, J. Bull, Behavior of prestressed beam strengthened with external tendons, Journal of Structural Engineering 126 (9) (2000) 1033–1044.

[6] T. Chan, T. Yung, A theoretical study of force identification using prestressed concrete bridges, Engineering Structures 22 (11) (2000) 1529 – 1537.

[7] S. Law, Z. Lu, Time domain responses of a prestressed beam and prestress identification, Journal of Sound and Vibration 288 (4-5) (2005) 1011–1025, cited By (since 1996) 23.

[8] K. Dai, S. Chen, Vibration of spun-cast prestressed concrete poles, in: Conference Proceedings of the Society for Experimental Mechanics Series, 2007.

[9] E. Hamed, Y. Frostig, Natural frequencies of bonded and unbonded prestressed beams - prestress force effects, Journal of Sound and Vibration 295 (1-2) (2006) 28 – 39.

[10] M. Saiidi, B. Douglas, S. Feng, Prestress force effect on vibration frequency of concrete bridges, Journal of Structural Engineering 120 (7) (1994) 2233–2241.

[11] T. Hop, The effect of degree of prestressing and age of concrete beams on frequency and damping of their free vibration, Materials and Structures 24 (1991) 210–220.

[12] Y. Zhang, R. Li, Natural frequency of full-prestressed concrete beam, Transactions of Tianjin University 13 (5) (2007) 354–359.

[13] J.-T. Kim, C.-B. Yun, Y.-S. Ryu, H.-M. Cho, Identification of prestress-loss in psc beams using modal information, Structural Engineering and Mechanics 17 (3 - 4) (2004) 467–482.

[14] D. Noble, M. Nogal, A. O'Connor, V. Pakrashi, Impact hammer testing on post-tensioned steel RHS sections; an investigation of the "Compression Softening" effect, in: Proceedings of Civil Engineering Research in Ireland Conference, Vol. I, Civil Engineering Research Association of Ireland, 2014, pp. 427–432.

[15] Z. Bažant, L. Cedolin, Discussion of "Free Vibration Behavior of Prestressed Beams" by K. Kanaka Raju and G. Venkateswara Rao (February, 1986, Vol. 112, No. 2), Journal of Structural Engineering 113 (9) (1987) 2087–2087.

[16] S. Jain, S. Goel, Discussion of "Prestress Force Effect on Vibration Frequency of Concrete Bridges" by M. Saiidi, B. Douglas, and S. Feng, Journal of Structural Engineering 122 (4) (1996) 459–460.

[17] G. Deák, Discussion of "Prestress Force Effect on Vibration Frequency of Concrete Bridges" by M. Saiidi, B. Douglas, and S. Feng, Journal of Structural Engineering 122 (4) (1996) 458–459.

[18] F. Bartlett, Discussion of "Free Vibration Behavior of Prestressed Beams" by K. Kanaka Raju and G. Venkateswara Rao (February, 1986, Vol. 112, No. 2), Journal of Structural Engineering 113 (9) (1987) 2085–2087.

[19] A. Dall'Asta, L. Dezi, Discussion of "Prestress Force Effect on Vibration Frequency of Concrete Bridges" by M. Saiidi, B. Douglas, and S. Feng, Journal of Structural Engineering 122 (4) (1996) 458–458.

[20] A. Kerr, On the dynamic response of a prestressed beam, Journal of Sound and Vibration 49(4) (1976) 569–573.

[21] M. S. Williams, S. Falati, Modal testing of a post-tensioned concrete model floor slab, Vol. 1, 1999, pp. 14–20, cited By (since 1996) 2.

[22] D.-D. Ho, J.-T. Kim, N. Stubbs, W.-S. Park, Prestress-force estimation in psc girder using modal parameters and system identification, Advances in Structural Engineering 15 (6) (2012) 997–1012, cited By (since 1996) 0.

[23] Z. Lu, S. Law, Identification of prestress force from measured structural responses, Mechanical Systems and Signal Processing 20 (8) (2006) 2186–2199, cited By (since 1996) 15.

[24] Y. Zhang, Y. Zheng, H. Li, A dynamic test of fully prestressed concrete beams, Advanced Materials Research 368 - 373 (2012) 2483–2490.

[25] MATLAB, version 8.3.0 (R2014a), The MathWorks Inc., Natick, Massachusetts, 2014.

[26] R. Clough, J. Penzien, Dynamics of Structures, Civil Engineering Series, McGraw-Hill, 1993.

[27] A. Chopra, Dynamics of Structures: Theory and Applications to Earthquake Engineering, Civil Engineering and Engineering Mechanics Series, Prentice Hall, 2012.

[28] B. Wu, A correction of the half-power bandwidth method for estimating damping, Archive of Applied Mechanics (2014) 1–6.

[29] British Standards, Eurocode 3: Design of steel structures Part 1-1: General rules and rules for buildings (May 2005).